Chinese Chemical Letters 37 (2026) 112449

Contents lists available at ScienceDirect

Chinese Chemical Letters

journal homepage: www.elsevier.com/locate/cclet

Activable chimeric bioluminescent sensors *via* electrostatic protein engineering for field-deployable imaging of wound infection

Junbin Li[a], Min Dai[a], Tianxin Zhang[a], Xindi Sun[b], Du Lian[a], Mengyi Xiong[b,*], Yibo Zhou[a], Zhihe Qing[a,*]

[a] *Hunan Provincial Key Laboratory of Cytochemistry, School of Chemistry and Pharmaceutical Engineering, Changsha University of Science and Technology, Changsha 410114, China*

[b] *Molecular Science and Biomedicine Laboratory (MBL), State Key Laboratory of Chemo/Biosensing and Chemometrics, College of Chemistry and Chemical Engineering, Hunan University, Changsha 410082, China*

ARTICLE INFO

Article history:
Received 21 July 2025
Revised 27 November 2025
Accepted 22 January 2026
Available online 23 January 2026

Keywords:
Fluorescent probe
Bioluminescent sensor
Protein engineering
Wound infection
Field-deployable imaging

ABSTRACT

Genetically encoded sensors have been extensively utilized for the analysis of biomarkers. However, their applications remain limited by the scarcity of analyte-binding proteins or peptides and the challenges associated with translating analyte recognition into a quantifiable signal. Herein, we report a novel class of activable chimeric sensors that harness bioluminescent resonance energy transfer (BRET) between nanoluciferase proteins and fluorescent small-molecule probes. We demonstrated that the responsiveness of these hybrid sensors can be significantly enhanced by modulating the electrostatic surface potential of the fusion protein in the vicinity of the recognition site. As proof of concept, we engineered two chimeric bioluminescent sensors, Bp7-pH and Bp7-NO, for the detection of pH and nitric oxide (NO), respectively. Both sensors exhibited strong BRET signal modulation upon exposure to their target analytes, leading to distinct and quantifiable shifts in luminescence color. Importantly, we successfully applied these sensors for field-deployable imaging of pH and NO dynamics in a murine wound infection model. Given the vast array of existing fluorescent molecular sensors, the detection targets of these chimeric bioluminescent sensors can be easily modified by altering the recognition moieties. Collectively, this work establishes a generalizable and tunable design strategy for developing highly sensitive chimeric bioluminescent sensors, with broad applicability in physiological and pathological monitoring.

© 2026 Published by Elsevier B.V. on behalf of Chinese Chemical Society and Institute of Materia Medica, Chinese Academy of Medical Sciences.

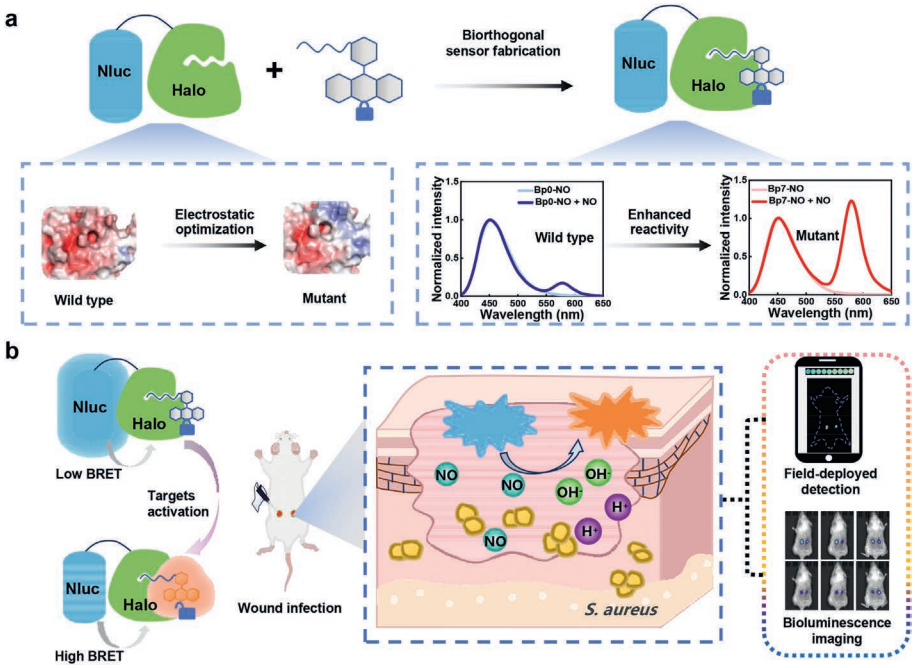
Genetically encoded sensors, featuring noninvasive and real-time imaging capability, have been widely developed to detect and visualize molecular and cellular biological processes [1–3]. Using specific peptides as recognition moieties to modulate the luminescence of protein of interest (POI) through protein-protein interactions or protein-ligand binding, these sensors have proved to be powerful tools for monitoring various biomarkers such as metal ions [4–6], amino acid [7] neurotransmitters [8,9], and nucleotide [10]. For bioactive species, particularly reactive oxygen species (ROS), unnatural amino acids with recognition groups are integrated into fluorescent proteins or firefly luciferase via genetic code expansion technology. The fluorescence or bioluminescence of the protein sensor is enhanced when the analyte undergoes a specific chemical reaction with the unnatural amino acid. While much progress has been made, this class of sensors can detect only a limited number of bioactive species, including H_2O_2 [11], H_2S [12], $ONOO^-$ [13,14], and formaldehyde [15]. The development of genetically encoded sensors for a broader range of bioactive species remains challenging. Therefore, expanding the applicability of genetically encoded sensors to detect a wider variety of bioactive species continues to be a significant research focus.

Semisynthetic genetically encoded sensors combine the features of genetic encoding with the versatility of synthetic chemistry, offering enhanced functionality in molecular detection [16,17]. The sensing mechanism typically relies on the competition between a tethered fluorescent ligand and the analyte for binding to a protein [18]. This hybrid approach enables the development of sensors with enhanced specificity, sensitivity, and functionality across many analytes, such as NAD^+ [19], NADPH [20], coenzyme A [21], and Acetyl-CoA [22]. Despite these advances, the detection range of current semisynthetic sensors is still limited by their recognition modules that are proteins or peptide chains.

Fluorescent molecular sensors, featured with precisely structural tunability [23–25], have been developed for highly spe-

* Corresponding authors.
E-mail addresses: xiongmy@hnu.edu.cn (M. Xiong), qingzhihe@hnu.edu.cn (Z. Qing).

https://doi.org/10.1016/j.cclet.2026.112449
1001-8417/© 2026 Published by Elsevier B.V. on behalf of Chinese Chemical Society and Institute of Materia Medica, Chinese Academy of Medical Sciences.



Scheme 1. (a) Schematic representation of the fabrication of highly activable chimeric bioluminescent sensors *via* surface electrostatic optimization. (b) Application of the sensors for field-deployable imaging of bioactive species during wound infection.

cific and real-time detection of diverse analytes, including reactive species [26–28], enzymes [29,30], and nucleic acid [31]. We explored the potential of combining small-molecule fluorescent sensors with genetically encoded proteins for the detection of bioactive species. Our group used to utilize synthetic molecular sensor as recognition modules in the fabrication of semisynthetic genetically encoded sensors [32]. However, the response capability of the recognition modules was abolished after implantation into the circular permutated Nanoluciferase-HaloTag fusion protein (cpHNLuc), for which the molecular sensors have to be activated prior to their labeling to the protein, severely hindering their applications complex systems. Therefore, there is a pressing need to explore a more universal strategy for the development of semisynthetic sensors.

Herein, we present a versatile and adaptable approach to develop chimeric bioluminescent sensors for ratiometric detection of reactive species. As depicted in Scheme 1, the sensor comprises the fusion protein cpHNLuc and an engineered molecular sensor. Their efficient bioorthogonal conjugation is achieved through a rapid, specific, and irreversible covalent reaction between the HaloTag domain in the cpHNLuc and the chloroalkane ligand anchored on the molecular sensor, which establishes precise spatial proximity and enables highly efficient bioluminescent resonance energy transfer (BRET). Our findings reveal that the electrostatic surface potential surrounding the synthetic molecular sensors on the protein significantly influences sensor reactivity. After systemic optimization of the surface electrostatic potential, a cpHNLuc variant was screened for constructing chimeric bioluminescent sensors. Given the strong correlation between changes in pH and nitric oxide (NO) levels with wound infection, we have developed two chimeric bioluminescent sensors for field-deployable and high signal-to-background ratio (SBR) imaging of pH and NO Both sensors exhibited strong BRET signal modulation upon target activation in the presence of the furimazine substrate, providing powerful tools for accurate and convenient assessment of wound status and adjustment of treatment strategies. Moreover, the modular design allows straightforward integration of diverse synthetic molecular sensors, making this platform readily adaptable for detecting a broad spectrum of biomarkers, which substantially extends the detection scope of conventional genetically encoded sensors.

To develop activity-based chimeric bioluminescent sensors with high sensitivity and robust imaging capabilities, several key criteria must be satisfied: (1) Efficient BRET between luciferase and fluorophore; (2) the small-molecule sensor labeled with luciferase retains excellent responsiveness to target analyte. In our previous study, efficient BRET bioluminescence detection system by systematically optimize the spectral overlap and the spatial distance between donor and acceptor. Unfortunately, the small-molecule sensor exhibited a markedly reduced response to analytes when embedded into the cpHNLuc scaffold [32]. We hypothesized that the local electrostatic surface potential surrounding the synthetic molecular sensors within the protein scaffold may significantly its reactivity [33]. Structural modeling displayed in Fig. S1 (Supporting information) revealed that the HaloTag labeling site of the original cpHNLuc0 was surrounded by negatively charged amino acid residues (AARs), including Glu144, Glu148, Asp339, Glu353, Glu366, and Glu368. This resulted in a strongly negative electrostatic environment, which may electrostatically repel negative charged analyte such as ClO^-.

To test this hypothesis, we evaluate the reactivity of chimeric bioluminescent sensors constructed from cpHNLuc variants engineered to possess different surface potentials. Specifically, a series of cpHNLuc variants (cpHNLuc1–cpHNLuc9) were designed by systematically replacing the negatively charged AARs in cpHNLuc0 with lysine (Table S1 in Supporting information), thereby introducing localized positive charges to reverse the electrostatic potential near the labeling site (Fig. 1a). As the number of substitutions increased, the calculated surface electrostatic potential gradually shifted from negative to positive (Fig. 1b). All cpHNLuc variants were successfully expressed in *Escherichia coli*, as confirmed by SDS-PAGE analysis (Fig. S2 in Supporting information).

Then, we designed and synthesized a small-molecule pH sensor, H-FITC (Scheme S1a in Supporting information). As expected, H-FITC showed significant pH-dependent enhancement in both absorption and fluorescence intensity across the pH range of 5.0-9.0 (Fig. S3 in Supporting information). This behaviour can

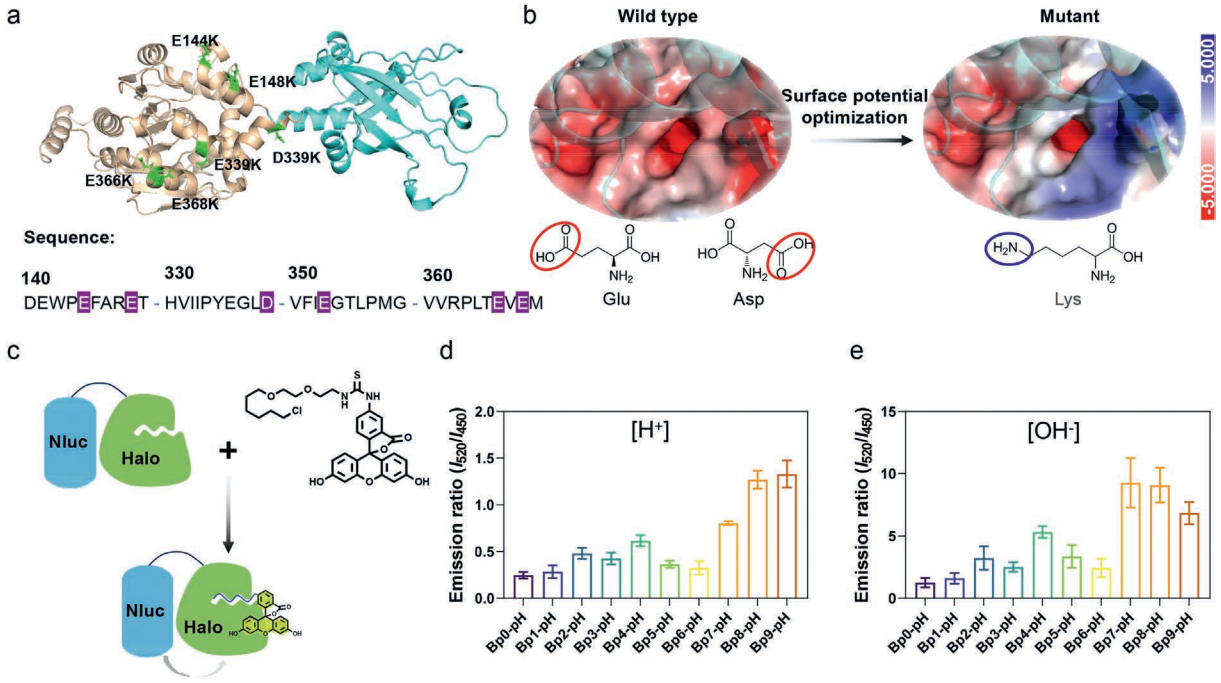


Fig. 1. Evolution of cpHNLuc for chimeric bioluminescent sensors construction. (a) Structure simulation of cpHNLuc0 and its mutation sites (marked as green). (b) Surface potential of the labeling site on cpHNLuc0 and its variant cpHNLuc7, with a color gradient from red to blue representing electrostatic potential from negative to positive. (c) The chloroalkane of H-FITC covalently conjugated to cpHNLuc variants to construct a series of chimeric pH bioluminescent sensors (Bp0-pH to Bp9-pH). The BRET ratio (I_{520}/I_{450}) of the sensors at pH 5.0 (d) and 9.0 (e). Data are shown as mean ± SD ($n = 3$).

be attributed to the protonation process occurring under low pH conditions, which promotes the formation of weakly fluorescent ring-closed spiroform. Conversely, under high pH conditions, deprotonation favours the formation of ring-open structures, thereby significantly enhancing fluorescence. Then, a series of semisynthetic pH-responsive bioluminescent sensors, named Bp0-pH to Bp9-pH, were developed from the corresponding proteins cpHNLuc0 to cpHNLuc9. This was achieved by covalently conjugating the chloroalkane group of H-FITC to the Asp106 residue of the cpHNLuc variants through a biorthogonal labeling reaction (Fig. 1c). Successful coupling of H-FITC to cpHNLuc was confirmed by SDS-PAGE analysis (Fig. S4 in Supporting information). Spectral analysis revealed strong overlap between the absorption spectrum of H-FITC and the bioluminescent emission spectrum of cpHNLuc0 (Fig. S5a in Supporting information). Bioluminescence spectrum of the Bp0-pH exhibited not only the characteristic Nanoluciferase emission peak at 450 nm, but also a strong new emission peak at 520 nm (Fig. S5b in Supporting information). This result indicates the occurrence of efficient BRET between the donor and acceptor components.

Next, we evaluated the pH responsiveness of the bioluminescent sensors. As shown in Figs. 1d and e, in an acidic environment (pH 5), the cpHNLuc0, which possesses a negatively charged surface, exhibited a relatively low BRET ratio. This likely due to the enhanced accessibility of protons (H^+) to the sensor, leading to quenching of FITC fluorescence. In contrast, cpHNLuc7, cpHNLuc8 and cpHNLuc9, which feature increasingly positively charged surfaces, showed higher BRET ratios under the same acidic conditions. The electrostatic repulsion between the positively charged protein surface and H^+ ions may reduce proton access to the FITC moiety, thereby mitigating fluorescence quenching. A similar trend was observed in an alkaline condition (pH 9), negatively charged cpHNLuc variants displayed weaker BRET signals compared to their positively charged counterparts. This may be attributed to repulsion between the negatively charged protein surface and hydroxide ions (OH^-), which restricts ion access to the sensor and results in a diminished FITC fluorescence enhancement. These findings suggest that substituting negatively charged AARs close to the labeling site with positively charged ones can improve sensor-analyte interactions by optimizing local electrostatic environments. Among these variants, cpHNLuc7 exhibited the largest BRET dynamic range and was therefore selected for the construction of subsequent chimeric bioluminescent sensors.

We then used the Bp7-pH bioluminescent sensor for both visual and quantitative detection of pH (Fig. 2a). Bioluminescence spectra of Bp7-pH were recorded in buffers solution with various pH. As shown in Fig. 2b, the emission intensity at 520 nm increased significantly as the pH rose from 5.0 to 9.0, resulting in approximately a 10-fold enhancement in the BRET ratio (I_{520}/I_{450}), from 0.73 to 7.17. The sensor exhibited an apparent p*K*a of 7.00 ± 0.02, making it well-suited for monitoring physiological pH variations (Fig. 2c). A major limitation of traditional bioluminescent probes is signal decay caused by substrate consumption, which hinders their applications in quantitative analysis. Our BRET overcomes this issue through self-calibration. As shown in Fig. 2d, the emission ratio (I_{520}/I_{450}) of Bp7-pH kept constant within 15 min at different pH (Fig. 2d). Additionally, a distinct bioluminescence color shift from blue to yellow was visually observed as the pH increased from 5.0 to 9.0 (Fig. 2e). These changes could be captured using a standard smartphone camera. Image analysis software was used to extract the green and blue channels, and the resulting green-to-blue intensity ratio served as a visual indicator for pH (Fig. 2f).

According to previous studies, the healthy skin typically has a slightly acidic pH, while infected or chronic wounds exhibit a significant higher pH [34,35], The skin pH can serve as a real-time indicator of wound healing processes. Regular monitoring of wound pH is essential for tracking healing progress, adjusting treatment protocols, simplifying care, and reducing patient stress. Therefore, we further developed simple cassettes for smartphone-based visual of wound pH by using Bp7-pH (Fig. 2g). The experimental

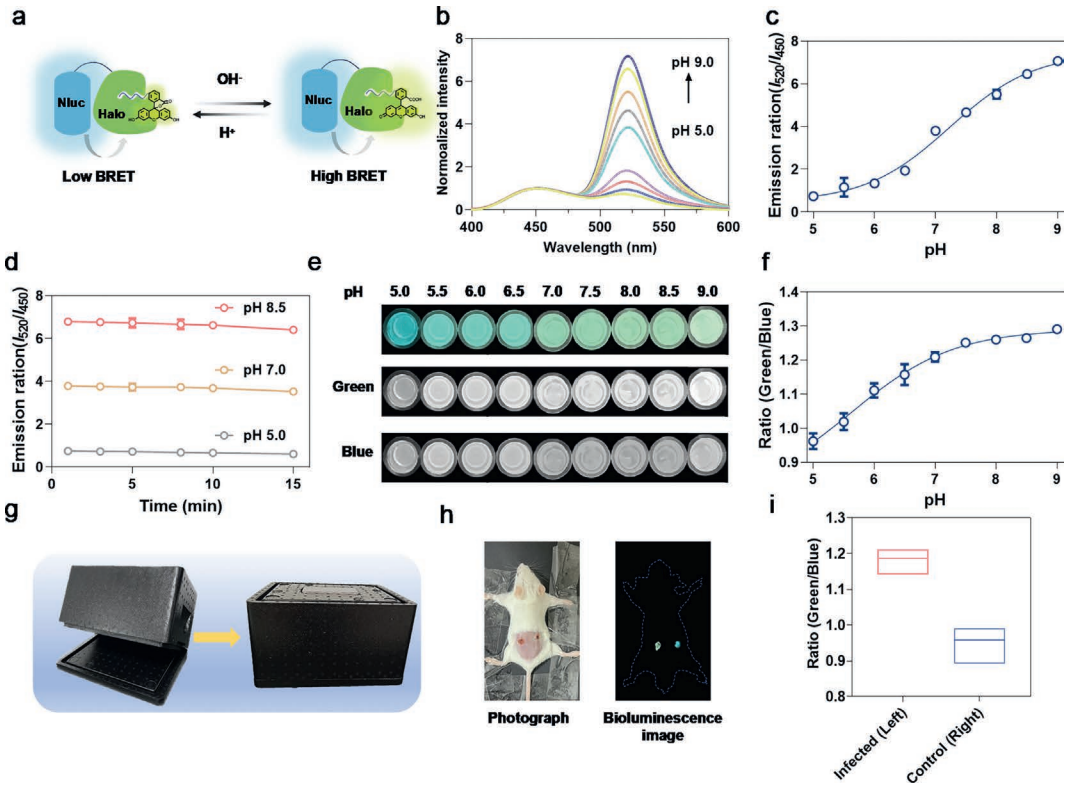


Fig. 2. (a) Schematic illustration of Bp7-pH for visual and quantitative pH detection. (b) Normalized bioluminescence spectra of Bp7-pH at different pH levels. (c) Plot of the emission intensity ratio (I_{520}/I_{450}) *versus*pH values in the range pH 5.0–9.0. (d) The emission ratio of Bp7-pH towards different pH over time (1–15 min) after the addition of furimazine (final concentration 50 μmol/L). (e) Bioluminescent images of Bp7-pH at various pH 5.0–9.0, with green and blue color channels separation by software. (f) The color ratio (green/blue) of Bp7-pH as a function of increasing pH. (g) Schematic illustration of the smartphone-based imaging device. (h) Photograph and bioluminescence image (after incubation with Bp7-pH) of a mouse with infected wound (left) and normal wound (right) using a smartphone. (i) The color ratio (green/blue) of the infected (left) and normal (right) wound. Data are shown as mean ± SD ($n = 3$).

procedures involving animals were approved by the Institutional Animal Care and Use Committee of Hunan University (No. SYXK 2022–0007). As the shown in Figs. 2h and i, bioluminescent emission of infected wound appeared more yellow, indicating a higher pH compared to normal wounds. These results demonstrate the bioluminescence-based ratiometric sensor Bp7-pH enables both visual and quantitative measurement of pH in complex samples.

To demonstrate the generalizability of this strategy, we designed and synthesized a NO sensor, H-TMR-NO. NO is a ubiquitous, uncharged free radical that serve as a key signaling molecule in both intracellular and intercellular communication, playing crucial roles in physiological and pathophysiological processes, such as inflammatory, cancer, and neurodegeneration diseases [36–39], Although numerous fluorescent sensors and a few bioluminescent turn-on sensors have been developed for NO detection (Table S2 in Supporting information) [40–44], the development of ratiometric bioluminescent sensors remains limited, hindering simultaneous visual and quantitative analysis of NO levels. To address this, we incorporated an *o*-phenylenediamine-based recognition moiety into a rhodamine scaffold to construct H-TMR-NO, followed by attachment of a chloroalkane linker via amide coupling (Scheme S1b in Supporting information). Upon exposure to NO, the sensor exhibited a new absorption band centered at 553 nm (Fig. S6a in Supporting information), along with a marked enhancement in fluorescence emission at 580 nm (Figs. S6b and c in Supporting information). Kinetic analysis showed that the reaction completion within 30 min (Fig. S6d in Supporting information). The fluorescence enhancement is attributed to the reaction of NO with the *o*-phenylenediamine group, forming a reactive benzotriazole intermediate that rapidly hydrolyzes to yield the fluorophore H-TMR. This transformation was further confirmed by mass spectrometry, which revealed a characteristic ion peak at $m/z = 636.5$, corresponding to H-TMR (Fig. S7 in Supporting information). Collectively, these results demonstrate that H-TMR-NO functions as an efficient and selective fluorescent probe for NO detection, supporting its integration into bioluminescent hybrid sensors. By conjugating H-TMR-NO with cpHNLuc0 to cpHNLuc9 variants, we constructed a panel of activity-based bioluminescent NO sensors (Bp0-NO to Bp9-NO), for both visual and quantitative detection of NO (Fig. 3a). As shown in Fig. S8 (Supporting information), SDS-PAGE analysis followed by Coomassie Brilliant Blue staining and in-gel fluorescence scanning confirmed the successful covalent coupling of H-TMR-NO to the cpHNLuc variants. We next assessed the bioluminescence response of each sensor to NO Among the variants, Bp7-NO, comprising cpHNLuc7 conjugated with H-TMR-NO, displayed the most significant response, exhibiting a 93-fold increase in the BRET ratio (I_{580}/I_{450}) upon treatment with 200 μmol/L NO (Fig. 3b). These finding indicate that Bp7-NO possesses high sensitivity toward NO and is well-suited for applications requiring robust ratiometric bioluminescent detection.

The response of Bp7-NO toward different concentrations of NO was next studied in HEPES buffer. With increasing NO concentration, bioluminescence emission at 580 nm showed a significant enhancement at normalized bioluminescence spectra (Fig. 3c). This indicates that more small-molecule probes were converted into fluorophores, leading to high BRET efficiency. Within the NO concentration range of 0 to 200 μmol/L, the sensor exhibited a concentration-dependent increase in the BRET ratio (I_{580}/I_{450}), which rose from 0.01 to 1.20 (Fig. 3d). The sensor exhibited excellent linear response ($R^2 = 0.992$) between 0.5–10.0 μmol/L, with

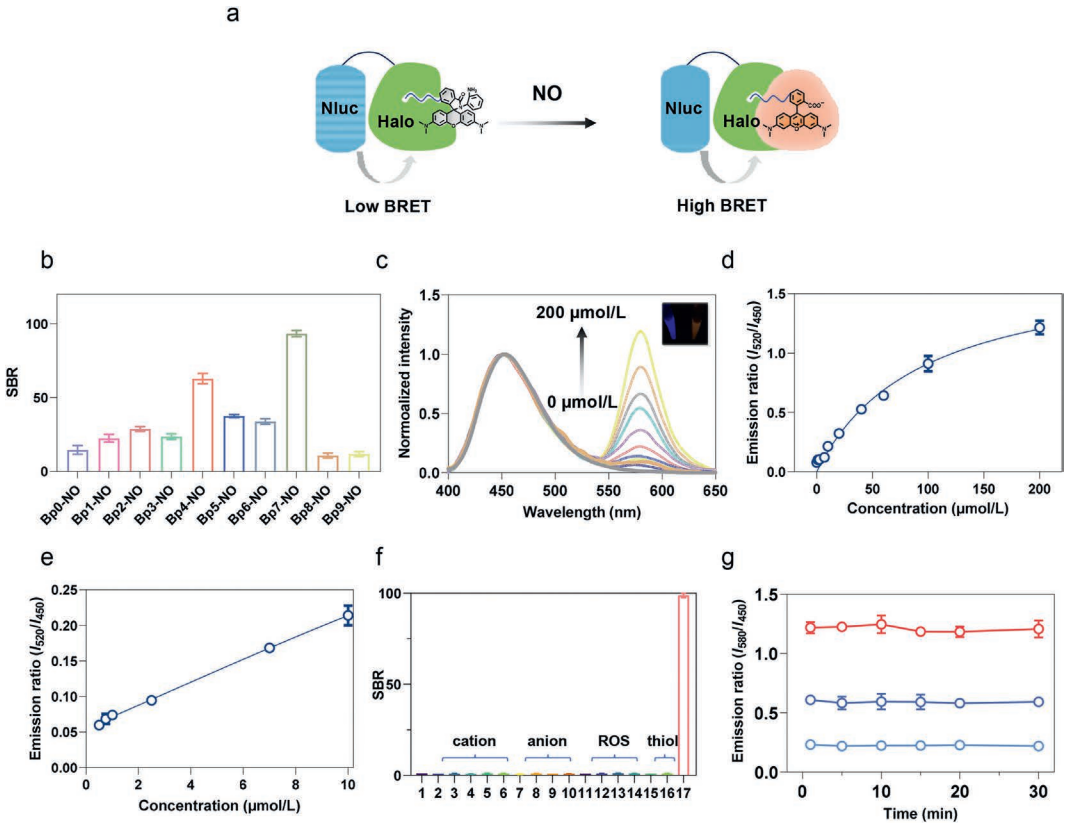


Fig. 3. (a) Schematic illustration of cpHNLuc-based bioluminescent sensors for NO detection. (b) The SBR of the bioluminescent sensors upon exposure to 200 μmol/L NO. (c) Normalized bioluminescence spectra of Bp7-NO with increasing NO concentrations (0–200 μmol/L). Inset: bioluminescent images of the Bp7-NO in the absence (left) and presence (right) of NO after adding furimazine substrate. (d) Emission ratio (I_{580}/I_{450}) of Bp7-NO as a function of NO concentration (0–200 μmol/L). (e) Linear fitting curve showing the relationship between emission ratio and NO concentration. (f) The SBR of Bp7-NO response to various kinds of biological molecules. (1) blank, (2) Mg^{2+} (1 mmol/L), (3) Ca^{2+} (1 mmol/L), (4) Fe^{3+} (1 mmol/L), (5) NH^{4+}(1 mmol/L), (6) Fe^{2+} (1 mmol/L), (7) $S_2O_3^{2-}$ (1 mmol/L), (8) SO_4^{2-} (1 mmol/L), (9) SO_3^{2-}(1 mmol/L), (10) NO_2^- (1 mmol/L), (11) H_2O_2 (200 μmol/L), (12) $ONOO^-$ (200 μmol/L), (13) $O_2^{\bullet-}$ (200 μmol/L), (14) $HO^\bullet$ (200 μmol/L), (15) Cys (1 mmol/L), (16) GSH (1 mmol/L), (17) NO (200 μmol/L). (g) Emission ratio of Bp7-NO at different NO concentrations over time (1–30 min) following the furimazine addition (final concentration: 50 μmol/L). Data are shown as mean ± SD ($n = 3$).

a calculated detection limit of 99 nmol/L (3σ/slope) (Fig. 3e). To assess specificity, the BRET response of Bp7-NO was measured in the presence of various potentially interfering species. As shown in Fig. 3f, only NO elicited a significant increase in emission at 580 nm, while no significant alteration in the BRET ratio was detected with other interfering substances, including cations (Mg^{2+}, Ca^{2+}, Fe^{3+}, NH^{4+}, Fe^{2+}), anions ($S_2O_3^{2-}$, SO_4^{2-}, SO_3^{2-}, NO_2^-), ROS (H_2O_2, $ONOO^-$, $O_2^{\bullet-}$, $HO^\bullet$), and biothiols (GSH, Cys). Furthermore, the emission ratio (I_{580}/I_{450}) remained stable over a 30 min period following addition of furimazine, at NO concentrations of 10, 60, and 200 μmol/L (Fig. 3g). These results collectively confirm that Bp7-NO is a highly selective, sensitive, and stable ratiometric bioluminescent sensor for quantitative NO detection.

Wound infections caused by pathogenic bacteria can significantly delay the wound healing and increase clinical burden. NO plays a concentration-dependent role in different stages of wound healing, so that elevating NO levels are characteristic of the inflammatory phase, whereas reduced levels indicate a transition to the proliferative phase [45,46]. Given its dynamic involvement, real-time *in vivo* monitoring of NO is crucial for evaluating wound status, guiding therapeutic strategies, and deepening our understanding of NO-mediated healing mechanisms.

Full-thickness, round skin wounds (~1.0 cm in diameter) were created on both sides of the dorsal surface in mice. Each wound was pretreated with 25 μL HEPES buffer containing 250 nmol/L Bp7-NO. The right wound was administered with 200 μmol/L NO, while the left wound was treated with an equal volume of HEPES buffer as a control. Following the addition of furimazine (1:50 dilution), bioluminescence signals from cpHNLuc7 (donor) and H-TMR (acceptor) were collected from the wound sites (Fig. 4a). Clear emissions from both cpHNLuc7 and H-TMR were detected. As shown in Fig. 4b, the BRET ratio in NO-treated wound exhibited a time-dependent increase, reaching a 2.6-fold enhancement compared to the control wound after 20 min. Although the absolute signal intensities of cpHNLuc7 and H-TMR varied slightly across different imaging time points, the BRET ratio in the control group remained stable throughout the experiment. These results confirm that the ratiometric bioluminescent sensor Bp7-NO effectively compensates for background fluctuations and enables reliable *in vivo* detection of NO.

To evaluate the capability of Bp7-NO for detecting endogenous NO, a bacterial infection wound model was established (Fig. 4c). The left wound was inoculated with *S. aureus* (1×10^6 CFU/mL), while the right wound received an equal volume of HEPES buffer as a negative control. After substrate addition, bioluminescence signals from cpHNLuc7 and H-TMR were collected and analyzed. As shown in Fig. 4d, the infected wounds exhibited a significantly higher BRET ratio compared to the uninfected controls, indicating elevated NO levels in response to bacterial infection. Notably, Bp7-NO enabled bioluminescence imaging with a SBR over 375-fold higher than that achieved by fluorescence imaging (Fig. S9 in Supporting information). These results highlight the excellent sensitivity and imaging contrast of Bp7-NO for monitoring endogenous NO levels during bacterial infection *in vivo*.

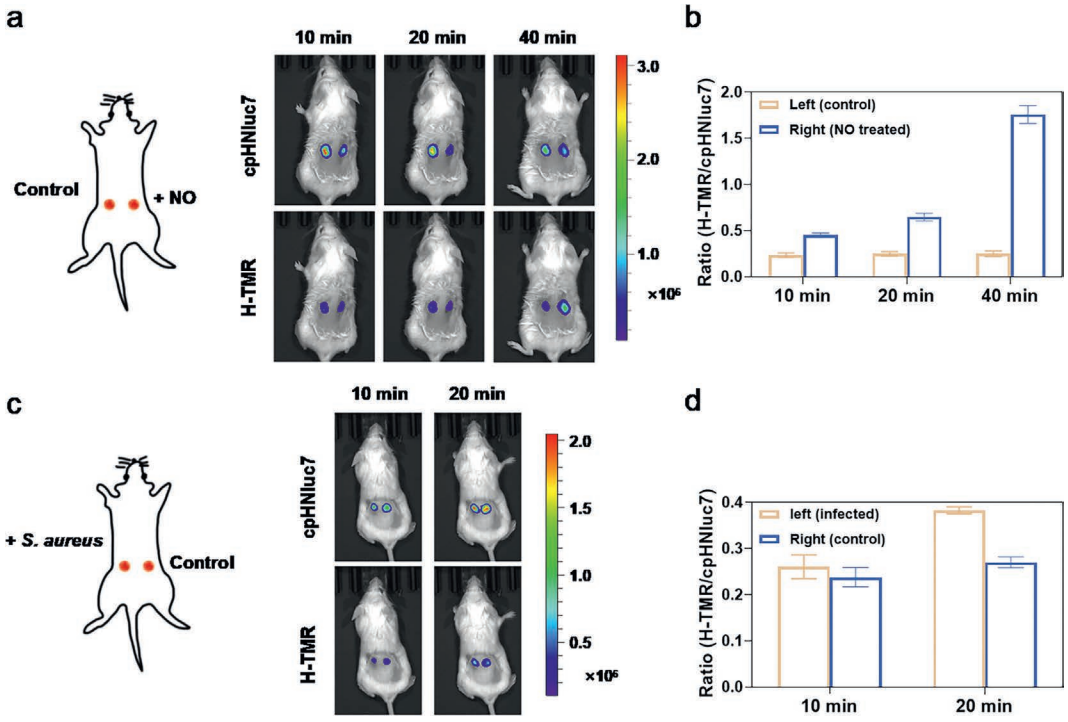


Fig. 4. The bioluminescent sensor Bp7-NO for sensing NO *in vivo*. (a) Schematic representation and bioluminescence imaging of BALB/c mouse wound model, showing treatment with or without NO (200 μmol/L) in the right or left wounds. (b) Quantification of the emission ratio (H-TMR/cpHNluc7) for each wound at different imaging time (10, 20, 40 min). (c) Illustration and bioluminescence imaging of mouse wound model infected with or without *S. aureus*, subsequently treated with Bp7-NO. (d) Quantification of the emission ratio (H-TMR/cpHNluc7) for each wound at different imaging time points (10 and 20 min). Data are shown as mean ± SD ($n = 3$).

In summary, we have developed a versatile platform of activable chimeric bioluminescent sensors for ratiometric detection of bioactive species. This strategy is based on rational engineering of a Nanoluciferase-HaloTag fusion protein, in which tuning the electrostatic surface potential significantly enhances the interaction efficiency between small-molecule probes and their target analytes. As a proof-of-concept, two representative sensors, Bp7-pH and Bp7-NO, were constructed for pH and NO detection. These sensors not only overcome the signal attenuation commonly associated with bioluminescent probes but also provide improved imaging accuracy and ratiometric robustness. Furthermore, their applicability was validated in a mouse wound infection model, demonstrating the potential for field-deployable *in vivo* monitoring of physiologically relevant analytes. Owing to the broad diversity of available fluorescent small-molecule probes, this modular design strategy can be readily extended to a wide range of targets, offering a powerful and generalizable approach to expand the toolkit of genetically encoded biosensors.

CRediT authorship contribution statement

Junbin Li: Writing – original draft, Supervision, Funding acquisition, Data curation, Conceptualization. **Min Dai:** Visualization, Methodology, Investigation. **Tianxin Zhang:** Visualization, Validation, Investigation. **Xindi Sun:** Software, Methodology, Investigation. **Du Lian:** Visualization, Validation. **Mengyi Xiong:** Writing – review & editing, Formal analysis, Data curation. **Yibo Zhou:** Validation, Resources, Methodology. **Zhihe Qing:** Writing – review & editing, Project administration, Funding acquisition.

Declaration of competing interest

The authors declare that they have no known competing financial interests or personal relationships that could have appeared to influence the work reported in this paper.

Acknowledgments

This work was supported by the National Natural Science Foundation of China (Nos. 22204008, 22222402, 22474012), and the Natural Science Foundation of Hunan Province (Nos. 2025JJ50080, 2024JJ3001).

Supplementary materials

Supplementary material associated with this article can be found, in the online version, at doi:10.1016/j.cclet.2026.112449.

References

[1] M. Wang, Y. Da, Y. Tian, Chem. Soc. Rev. 52 (2023) 1189–1214.
[2] Y. Nasu, C. Murphy-Royal, Y. Wen, et al., Nat. Commun. 12 (2021) 7058.
[3] M. Cui, D. Wang, X.E. Zhang, et al., Sci. Sin. Chim. 52 (2022) 1699–1711.
[4] M. Xiong, Z. Yang, R.J. Lake, et al., Angew. Chem. Int. Ed. 59 (2020) 1891–1896.
[5] A.P. Torres-Ocampo, A.E. Palmer, Curr. Opin. Chem. Biol. 74 (2023) 102284.
[6] Y. Xian, M. Zhou, S. Han, et al., Chin. Chem. Lett. 31 (2020) 468–472.
[7] C. Wang, X. Zhang, H. Mao, et al., ACS Sens. 10 (2025) 1260–1269.
[8] J. Wan, W. Peng, X. Li, et al., Nat. Neurosci. 24 (2021) 746–752.
[9] H. Dong, Z. Wang, Y. Li, Cobehav. Sci. 62 (2025) 101489.
[10] M. Zhang, B. Yang, J. Zhang, et al., Angew. Chem. Int. Ed. 61 (2022) e202201266.
[11] O.M. Subach, T.A. Kunitsyna, O.A. Mineyeva, et al., Int. J. Mol. Sci. 20 (2019) 3138.
[12] S. Chen, Z.J. Chen, W. Ren, H.W. Ai, J. Am. Chem. Soc. 134 (2012) 9589–9592.
[13] Z. Chen, S. Zhang, X. Li, H.W. Ai, Cell Chem. Biol. 28 (2021) 1542–1553.e5.
[14] Y. Pang, M. Huang, Y. Fan, et al., ACS Chem. Biol. 18 (2023) 1388–1397.
[15] Y. Zhang, Y. Du, M. Li, et al., Angew. Chem. Int. Ed. 59 (2020) 16352–16356.
[16] S.I. Reja, M. Minoshima, Y. Hori, K. Kikuchi, Biosens. Bioelectron. 247 (2024) 115862.
[17] N. Mertes, M. Busch, M.-C. Huppertz, et al., J. Am. Chem. Soc. 144 (2022) 6928–6935.
[18] H. Farrants, J. Hiblot, R. Griss, K. Johnsson, Methods Mol. Biol. 1596 (2017) 101–117.
[19] Q. Yu, N. Pourmandi, L. Xue, et al., Nat. Metab. 1 (2019) 1219–1225.
[20] Q. Yu, L. Xue, J. Hiblot, et al., Science 361 (2018) 1122–1126.
[21] L. Xue, P. Schnacke, M.S. Frei, et al., Nat. Chem. Biol. 19 (2023) 346–355.
[22] W.K. Lieberman, Z.A. Brown, D.S. Kantner, et al., J. Am. Chem. Soc. 145 (2023) 16899–16905.

[23] L. Wu, Z. Li, K. Wang, et al., J. Am. Chem. Soc. 147 (2025) 9001–9018.
[24] S. Zeng, X. Liu, Y.S. Kafuti, et al., Chem. Soc. Rev. 52 (2023) 5607–5651.
[25] L. Wang, X. Liang, H. Chi, W. Lin, Chin. Chem. Lett. 36 (2025) 110962.
[26] Z. Zhao, W. Xiang, W. Guo, B. Wang, Anal. Chem. 97 (2025) 2127–2135.
[27] Y. Geng, Z. Wang, J. Zhou, et al., Chem. Soc. Rev. 52 (2023) 3873–3926.
[28] K.G. Fosnacht, M.D. Pluth, Chem. Rev. 124 (2024) 4124–4257.
[29] Y. Hu, J. Liu, M. Xu, K. Pu, J. Am. Chem. Soc. 147 (2025) 7148–7157.
[30] M. Zhao, Y. Chen, C. Zhang, et al., Chin. Chem. Lett. 37 (2026) 111061.
[31] J. Yang, Z. Xu, L. Yu, et al., Angew. Chem. Int. Ed. 63 (2024) e202318800.
[32] J. Li, N. Wang, M. Xiong, et al., Anal. Chem. 95 (2023) 7142–7149.
[33] M. Xiong, Y. Wu, G. Kong, et al., Angew. Chem. Int. Ed. 62 (2023) e202308086.
[34] E.M. Jones, C.A. Cochrane, S.L. Percival, Adv. Wound Care 4 (2015) 431–439.
[35] M. Lu, X. Zhang, D. Xu, et al., Adv. Mater. 35 (2023) 2211330.
[36] R.R. Zhang, X.Y. Ran, K.K. Yu, et al., Adv. Mater. 37 (2025) 2415891.
[37] Z. Jiang, Z. Liang, Y. Cui, et al., J. Am. Chem. Soc. 145 (2023) 7952–7961.
[38] M.E. Inda-Webb, M. Jimenez, Q. Liu, et al., Nature 620 (2023) 386–392.
[39] J. Huang, M. Xu, P. Cheng, et al., Angew. Chem. Int. Ed. 63 (2024) e202319780.
[40] L. Zhou, Z. Wang, L. Wang, et al., J. Am. Chem. Soc. 145 (2023) 28296–28306.
[41] A.K. Yadav, M.C. Lee, M.Y. Lucero, et al., ACS Cent. Sci. 8 (2022) 461–472.
[42] X. Ren, S. Han, Y. Li, et al., Anal. Chem. 96 (2024) 8689–8695.
[43] Y. Wen, X. Wu, W. Wu, et al., Anal. Chem. 96 (2024) 6666–6673.
[44] Q. Xu, Y. Zhang, M. Zhu, et al., Chem. Sci. 14 (2023) 4091–4101.
[45] S. Hassan, C.C. Schreib, X. Zhao, et al., ACS Sens. 7 (2022) 2253–2261.
[46] J. Wang, Z. Gao, H. Liang, et al., Chin. Chem. Lett. 36 (2025) 110569.